Microbial Cell Factories

RESEARCH

Open Access

Repurposing the Sb(III)-specific efflux and sequestration system (*ant* operon) to mitigate antimonite cross-talk in ArsR-based bacterial arsenite sensors

Jingwen Ling[1,2†], Yan Guo[2*†], Mingqi Liu[2,3], Jianpei Yun[2], Boxin Li[2], Xueqin Yang[2], Xuli Wu[1*] and Chang-ye Hui[1,2*]

Abstract

Background ArsR-based whole-cell biosensors offer sensitive colorimetric detection of arsenite [As(III)], yet their broad reactivity toward Group 15 metalloids—especially antimonite [Sb(III)]—limits field specificity. The recently identified *ant* operon from *Comamonas testosteroni* JL40 confers Sb(III)-selective resistance via the efflux ATPase AntA, the metallochaperone AntC, and the regulator AntR, providing genetic parts to suppress Sb(III) cross-talk.

Results We systematically introduced *antA*, *antC*, and three *antR* homologs into an ArsR regulator coupled with a deoxyviolacein reporter chassis (pJ23119-K12). Co-expression of AntA and AntC under a moderate constitutive promoter (P*ceuR*) shifted the Sb(III) limit of detection (LOD) from 0.073 μM to 0.586 μM, with a modest increase in the As(III) LOD to 0.018 μM. Subsequent integration of AntR1 not only maintained the As(III) LOD at 0.018 μM but also unexpectedly amplified the As(III) signal, extending the linear range to 36 nM–37.5 μM ($R^2 = 0.991$). It suggests that AntR1 may modulate the transcriptional circuitry via cross-regulation, warranting further mechanistic inquiry. The modified biosensor TOP10/pJ23119-antACR1 exhibited high selectivity for As(III) over divalent metals (Cd, Pb, Cu, Hg, Mn, Mg) and tolerated Sb(III) up to 1 μM. Performance was retained in 90% freshwater and 50% seawater matrices, enabling accurate quantification of 0–2.5 μM As(III) in deionized, tap, surface, and marine samples.

Conclusion By coupling Sb(III)-specific *ant* efflux/sequestration components with an ArsR-based sensing module, we developed a portable, low-cost biosensor that overcomes longstanding As(III)/Sb(III) cross-reactivity and performs robustly in complex environmental waters.

†Jingwen Ling and Yan Guo have contributed equally to this work.

*Correspondence:
Yan Guo
Yanguo615@163.com
Xuli Wu
wxl@szu.edu.cn
Chang-ye Hui
hcy_sypu@hotmail.com

Full list of author information is available at the end of the article

© The Author(s) 2025. **Open Access** This article is licensed under a Creative Commons Attribution-NonCommercial-NoDerivatives 4.0 International License, which permits any non-commercial use, sharing, distribution and reproduction in any medium or format, as long as you give appropriate credit to the original author(s) and the source, provide a link to the Creative Commons licence, and indicate if you modified the licensed material. You do not have permission under this licence to share adapted material derived from this article or parts of it. The images or other third party material in this article are included in the article's Creative Commons licence, unless indicated otherwise in a credit line to the material. If material is not included in the article's Creative Commons licence and your intended use is not permitted by statutory regulation or exceeds the permitted use, you will need to obtain permission directly from the copyright holder. To view a copy of this licence, visit http://creativecommons.org/licenses/by-nc-nd/4.0/.

Graphic

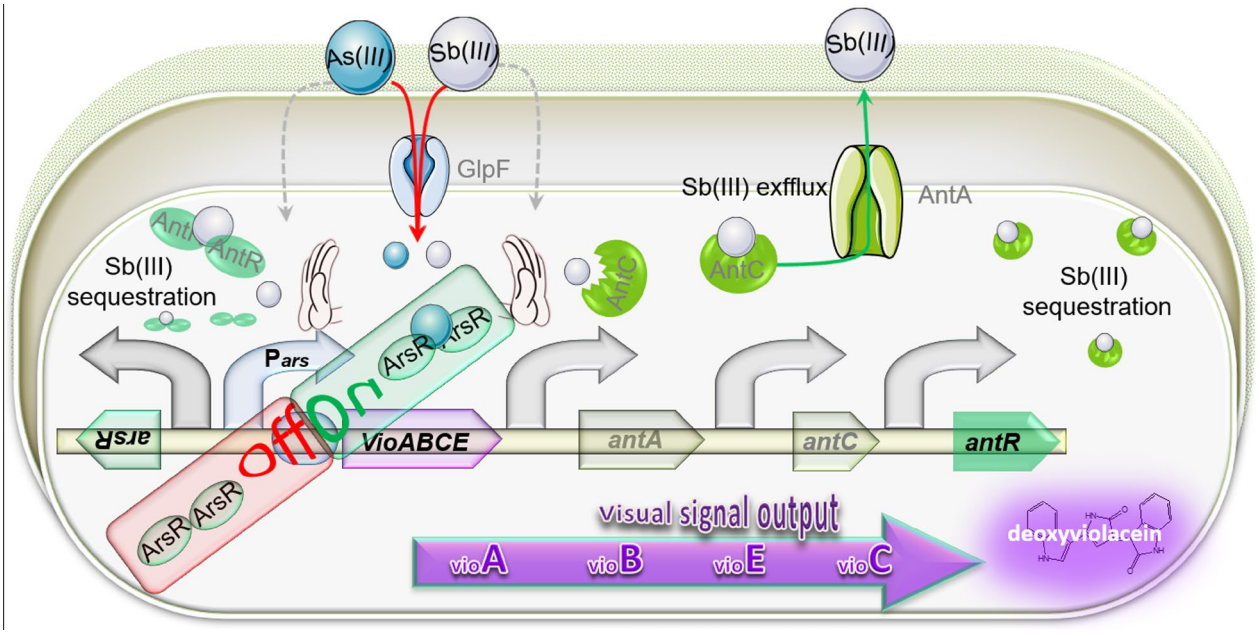

Keywords Arsenite detection, Whole-cell biosensor, Sb(III)-specific efflux, Sb(III) sequestration, *Ant* operon, As(III) selectivity.

Introduction

Arsenic (As) is the 20th most abundant metalloid in the Earth's crust. It is released into the hydrosphere through geogenic processes—such as volcanic emissions and hydrothermal activity—and anthropogenic activities, including mining, coal combustion, and groundwater over-extraction [1]. In aquatic environments, inorganic arsenic predominates as arsenite [As(III)] and arsenate [As(V)], with As(III) being more mobile, bioavailable, and toxic [2]. Chronic exposure to As(III), even at low μg/L levels, is associated with skin lesions, cardiovascular disease, and multiple cancers [3]. Consequently, the World Health Organization (WHO) has set a drinking-water guideline of 10 μg/L, and many countries apply the same limit to surface and groundwater monitoring programmes [4].

The gold-standard determination of arsenic relies on instrumental techniques that achieve sub-ppb sensitivity and speciation capability but demand expensive equipment, skilled operators, and centralized laboratories [5]. A spectrum of alternative methods has emerged to overcome these limitations, among which whole-cell biosensors are attracting intense interest. These biosensors genetically couple a sensory module (usually the ArsR repressor and its cognate operator) to a reporter module (fluorescent proteins, luciferases, or pigment enzymes) in living bacteria [6]. During the past decade, dozens of ArsR-based sensors have been constructed in *Escherichia coli*, *Bacillus subtilis*, and *Pseudomonas* spp., offering rapid, reagent-free, and field-deployable detection [7–9].

Our recent review systematically surveyed the synthetic-biology toolbox that transforms natural *ars* operons into tailored bacterial biosensors [6]. We highlighted how promoter/operator engineering, repressor titration, and positive-feedback loops suppress background noise, and we emphasized the unique advantages of pigment-synthetic pathways—such as violacein [10], indigoidine [11], and indigo [12] biosynthesis—that combine enzymatic amplification with naked-eye readout. Building on these design rules, our subsequent study screened six *ars* templates and identified the chromosomal *ars* operon of *E. coli* K12 as the optimal scaffold. We achieved a deoxyviolacein (DV)-based sensor exhibiting 1 nM sensitivity and a linear range (36 nM–1.17 μM) that straddles the WHO guideline [13]. However, like all ArsR-based devices [11, 14, 15], the sensor cross-reacts with Sb(III) and, to a lesser extent, Bi(III), compromising its selectivity for Group 15 metalloids.

To mitigate cross-reactivity of transcriptional regulators-based biosensors, previous efforts have pursued three complementary strategies: (i) promoter and repressor evolution to reshape the metal-binding pocket of metalloregulators [16–19]; (ii) incorporation of competing metalloregulators or anti-repressors that

preferentially bind the interfering ion [20, 21]; and (iii) metabolic rewiring to enhance intracellular sequestration or efflux of the interferent [22]. However, Previous studies have reported LOD ratios for As(III) and Sb(III) that are insufficient for selective detection in complex environmental samples [13, 15, 16]. A novel strategy offering enhanced Sb(III) discrimination is therefore warranted. Our study aims to improve these limitations by introducing the ant operon, which significantly enhances the selectivity for As(III) over Sb(III).

Table 1 Bacterial strains and plasmids used in this study

Strains and plasmids	Genotypes or description	Reference
E. coli strains		
TOP10	F⁻ Φ80*lac*ZΔM15 Δ*lac*X74 *rec*A1	Invitrogen
Plasmids		
pJ23119-K12	The *vioABCE* gene cluster fused downstream of a redesigned arsenic sensory element from *Escherichia coli* K12 chromosomal *ars* operon, the expression of *arsR* is under the control of constitutive PJ23119 promoter.	[13]
pJ23119-antA	pJ23119-K12 derivative with *antA* fused downstream of the *vioABCE* gene cluster, and the expression of AntA is control by the constitutive P*ceuR* promoter.	This study
pJ23119-antC	pJ23119-K12 derivative with *antC* fused downstream of the *vioABCE* gene cluster, the expression of AntC is controlled by the constitutive P*ceuR* promoter.	This study
pJ23119-antAC	pJ23119-K12 derivative with *antA* and *antC* fused downstream of the *vioABCE* gene cluster, the expression of AntA and AntC is controlled by the constitutive P*ceuR* promoter.	This study
pJ23119-HAntAC	pJ23119-K12 derivative with *antA* and *antC* fused downstream of the *vioABCE* gene cluster, the expression of AntA and AntC is controlled by the PJ23119 promoter.	This study
pJ23119-antACR1	pJ23119-antAC derivative with *antR1* fused downstream of the *antAC* gene cluster, the expression of AntR1 is controlled by the constitutive P*ceuR* promoter.	This study
pJ23119-antACR2	pJ23119-antAC derivative with *antR2* fused downstream of the *antAC* gene cluster, the expression of AntR2 is controlled by the constitutive P*ceuR* promoter.	This study
pJ23119-antACR3	pJ23119-antAC derivative with *antR3* fused downstream of the *antAC* gene cluster, the expression of AntR3 is controlled by the constitutive P*ceuR* promoter.	This study

Here, we introduce the *ant* operon of *Comamonas testosteroni*—an Sb(III)-specific resistance system—as a genetic firewall within an ArsR-DV biosensor chassis. By co-expressing the Sb(III)-efflux ATPase AntA, the metallochaperone AntC, and the regulator AntR, we selectively deplete intracellular Sb(III) without compromising As(III) sensitivity. This *ant-ars* cross-operon engineering yields a sensor that retains a nanomolar level sensitivity for As(III) while suppressing Sb(III)-mediated false positives by >4-fold, enabling accurate and portable arsenic monitoring in freshwater, tap water, and seawater. Our study demonstrates that leveraging natural resistance operons in tandem, such as the *ant–ars* cross-talk demonstrated here, provides a promising approach for developing next-generation whole-cell sensors. This method enhances Sb(III) discrimination and offers tunable specificity, expanded dynamic range, and robust performance in complex environmental matrices, without the need for resource-intensive evolution or instrumentation. Future work could investigate the applicability of this strategy to additional metal pairs to validate its potential further.

Materials and methods

Strains, plasmids, cultivation conditions, and chemicals

The bacterial strains and plasmid constructs employed in this study are listed in Table 1. *Escherichia coli* (*E. coli)* TOP10 was the host for all recombinant plasmids. Cultures were grown aerobically in Luria–Bertani (LB) medium (10 g/L tryptone, 5 g/L yeast extract, and 10 g/L NaCl) at 37 °C with orbital shaking at 250 rpm. Where indicated, ampicillin was added to a final concentration of 50 μg mL^{-1} to maintain plasmid selection.

Metal ion stock solutions of Mg(II), Cd(II), Hg(II), Mn(II), Pb(II), Cu(II), As(III), and Sb(III) were prepared fresh in ultrapure water from analytical-grade salts (Aladdin Reagent Co., Shanghai, China). Oligonucleotide primers and synthetic gene fragments were synthesized and sequence-verified by Sangon Biotech Co., Ltd. (Shanghai, China).

Construction of the sensing plasmid

Plasmid pJ23119-K12 was previously constructed [13] as the parent construct for all arsenic-responsive biosensors described in this study. The plasmid map of pJ23119-K12 is shown in Fig. S1, and the key components of plasmid pJ23119-K12 are summarized in Table S1. This vector contains a decoupled arsenic sensory module derived from the chromosomal *ars* operon of *E. coli* K-12, where the native resistance genes have been replaced with a truncated violacein biosynthesis operon, specifically vioABCE (see Fig. 1). In the absence of arsenite [As(III)] or antimonite [Sb(III)], dimeric ArsR binds to the ArsR-binding site (ABS) located within the Pars

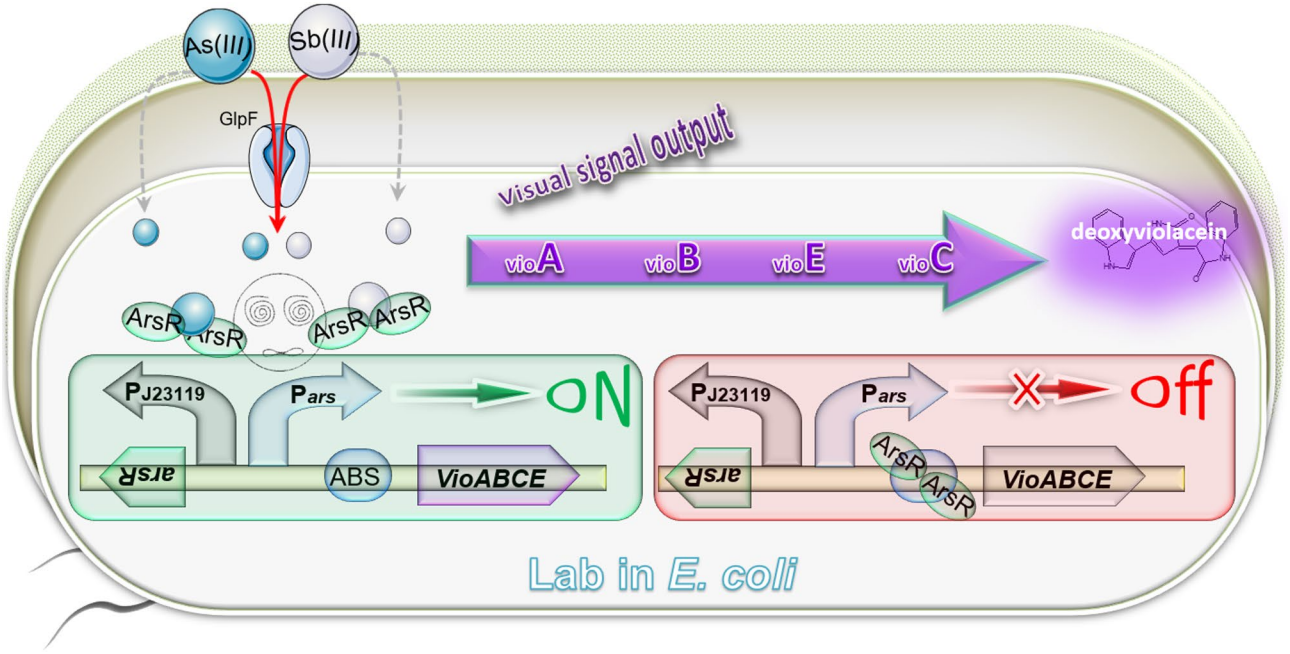

Fig. 1 Limitation of ArsR-based whole-cell biosensors. Schematic of pJ23119-K12. The strong constitutive PJ23119 promoter drives high-level expression of ArsR, ensuring tight repression of *vioABCE* via ABS binding. As(III) and Sb(III) induce ArsR dissociation from ABS, triggering DV synthesis. The lack of selectivity for Group 15 metalloids remains an unresolved challenge in arsenic biosensing

promoter, thereby repressing transcription of *vioABCE*. Upon intracellular accumulation of either metalloid, ArsR undergoes a conformational change that reduces its DNA-binding affinity, leading to dissociation from ABS and subsequent expression of *vioABCE*. The resulting deoxyviolacein (DV) pigment is quantitatively correlated with the concentration of As(III) or Sb(III), enabling colorimetric detection.

Despite its low background signal, pJ23119-K12 exhibits non-selective activation by both As(III) and Sb(III) (Fig. 1). This cross-reactivity is attributed to the inability of ArsR to discriminate between Group 15 metalloids, such as As(III), Sb(III), and Bi(III), representing a long-standing limitation of ArsR-based whole-cell biosensors [6, 14].

All derivative plasmids were engineered from pJ23119-K12 to attenuate the non-specific response to Sb(III). Two complementary strategies were adopted: (i) selective extrusion of intracellular Sb(III) via the Sb(III)-specific AntA P-type ATPase, and (ii) intracellular sequestration of Sb(III) by the metallochaperone AntC and its cognate regulator AntR.

To this end, we *de novo* synthesized the *antA* and *antC* expression cassettes under the control of the moderate constitutive promoter P*ceuR*. Each cassette was inserted into the *Sac*I–*Hind*III sites of pJ23119-K12, yielding pJ23119-antA and pJ23119-antC, respectively. The bicistronic *antA-antC* cassette was assembled downstream of P*ceuR* and cloned into the same sites, generating pJ23119-antAC.

Subsequent constructs were derived from pJ23119-antAC as follows: The P*ceuR* promoter driving *antA*/*antC* was swapped for the strong constitutive promoter PJ23119 to enhance Sb(III) efflux capacity to generate pJ23119-HAntAC. The PJ23119 promoter is a commonly used strong synthetic biology promoter known for its high-level expression capabilities [23]. The *antR1*, *antR2*, or *antR3* genes (encoding AntR homologs) were inserted downstream of *antA*–*antC* via the *Xho*I site under P*ceuR* control to bolster intracellular Sb(III) sequestration to generate pJ23119-antACR1/2/3.

All plasmids were introduced into *E. coli* TOP10 by chemical transformation using the $CaCl_2$ method. Transformants, the corresponding whole-cell biosensors, were selected on LB agar plates containing 50 μg/mL ampicillin after incubation at 37 °C overnight to obtain single colonies. The DNA sequences of all functional modules are provided in Table S1, and the origins of key proteins are summarized in Table S2.

Comparative As(III) and Sb(III) response profiles of engineered biosensors

To systematically evaluate the As(III) and Sb(III) response characteristics of the engineered whole-cell biosensors, eight freshly transformed *E. coli* TOP10 strains—TOP10/pJ23119-K12, TOP10/pJ23119-antA, TOP10/pJ23119-antC, TOP10/pJ23119-antAC, TOP10/

pJ23119-HAntAC, TOP10/pJ23119-antACR1, TOP10/pJ23119-antACR2, and TOP10/pJ23119-antACR3—were individually pre-cultured overnight in LB medium supplemented with 50 μg mL^{-1} ampicillin. Each overnight culture was then diluted 1:100 (v/v) into fresh LB containing the same antibiotic and exposed to a twice diluted of As(III) or Sb(III) concentrations: 0, 0.001, 0.002, 0.0045, 0.009, 0.018, 0.036, 0.073, 0.146, 0.293, 0.586, 1.171, 2.344, 4.688, 9.375, 18.75, 37.5, 75, and 150 μM. Cultures were incubated at 37 °C with orbital shaking (250 rpm) for 4 h. Following exposure, bacterial density (OD_{600}) and DV pigment accumulation (absorbance at 570 nm in n-butanol extracts) were quantified as previously described [24, 25].

Metal-selectivity assay of the optimized biosensor

To assess the metal selectivity of the optimized biosensor, overnight cultures of TOP10/pJ23119-antACR1 were diluted 1:100 (v/v) into fresh LB medium containing 50 μg mL^{-1} ampicillin. A two-fold dilution series was used to supplement the medium with Mg(II), Cd(II), Hg(II), Mn(II), Pb(II), Cu(II), Sb(III), or As(III) at final concentrations of 0, 0.15, 1.2, and 2.4 μM. Cultures were incubated at 37 °C with orbital shaking (250 rpm) for 4 h, after which bacterial density (OD_{600}) and DV pigment signal (A_{570}) were measured.

Interference resistance assay

To evaluate the interference resistance of the optimized biosensor TOP10/pJ23119-antACR1, overnight cultures were diluted 1:100 (v/v) into LB medium containing 50 μg mL^{-1} ampicillin. Individual metal solutions of Mg(II), Cd(II), Hg(II), Mn(II), Pb(II), Cu(II), and Sb(III) were added to final concentrations of 0.5 or 1.0 μM, followed by spiking with As(III) to 0.15 μM. Cultures were incubated at 37 °C with orbital shaking (250 rpm) for 4 h, after which bacterial density (OD_{600}) and DV pigment signal (A_{570}) were measured.

Evaluation of biosensor performance in environmental water matrices

Environmental water samples—including laboratory-prepared deionized water, municipal tap water, surface water from Donghu Park (Luohu District, Shenzhen, Guangdong, China), and seawater from Daya Bay (Yantian District, Shenzhen, Guangdong, China)—were collected for matrix compatibility testing. Each sample was clarified by centrifugation at 10,000 × g for 10 min, and the supernatant was sterilized by passage through a 0.22 μm membrane filter (Millipore, Billerica, MA, USA). Detection media were prepared as described previously [13, 26, 27] by mixing the clarified water samples with 10× LB broth, 10× NaCl-free LB broth, and sterile deionized water, following the volume ratios outlined in Table 2.

Table 2 A detection culture system for analyzing environmental water samples

Component	deionized water	Tap water	Surface water	Seawater
Water samples	90%	90%	90%	50%
10× LB	10%	10%	10%	-
10× NaCl-free LB	-	-	-	10%
Sterile water	-	-	-	40%

Overnight cultures of TOP10/pJ23119-antACR1 were diluted 1:100 (v/v) into the detection media prepared as described above and containing 50 μg mL^{-1} ampicillin. As(III) was introduced via a two-fold dilution series to achieve final concentrations of 0, 0.156, 0.313, 0.625, 1.25, 2.5, 5, and 10 μM. Cultures were incubated at 37 °C with orbital shaking (250 rpm) for 4 h, after which bacterial density (OD_{600}) and DV pigment signal (A_{570}) were quantified.

Under the guidance of the regression equation derived from the DV signals of As(III)-spiked samples, the concentrations of As(III) in three types of environmental water samples—tap water, surface water, and seawater—were determined after spiking with As(III) to final concentrations of 0.2 and 0.6 μM. The sensing and detection were performed using the TOP10/pJ23119-antACR1 biosensor, and the results were validated against total arsenic measurements obtained by atomic fluorescence spectrometry (AFS-9530 Haiguang Instrument, Beijing, China).

Statistical analysis

All statistical analyses were performed using IBM SPSS Statistics 26.0, and data visualization was generated with OriginPro 2024. Experiments were conducted in at least three independent biological replicates, and results are presented as mean ± standard deviation (SD). Two-tailed Student's t-test evaluated differences between two groups. In contrast, comparisons among multiple groups were carried out using one-way analysis of variance (ANOVA) followed by Tukey's post-hoc test. A significance level of $\alpha = 0.05$ was applied unless otherwise stated. The limit of detection (LOD) was calculated as described previously [28] using the following equations: Limit of blank (LOB) = mean_blank + 1.645 × SD_blank; LOD = LOB + 1.645 × SD_low-concentration sample.

Results and discussion

Engineering the Sb(III)-responsive *ant* Operon to enhance As(III) selectivity of ArsR-based biosensors

The *ars* operon is the most widespread arsenic-resistance system found in bacterial plasmids, transposons, and chromosomes, and it has become the predominant

template for developing arsenic biosensors [6]. Nevertheless, ArsR-based whole-cell biosensors typically exhibit cross-reactivity toward Group 15 metalloids (As(III), Sb(III), and Bi(III)) [7, 11]. By comparatively evaluating six distinct *ars* templates, our previous work identified the *E. coli* K-12 ArsR variant as the most promising scaffold, delivering high sensitivity and a broad As(III) detection window [13]. Background leakage, a persistent obstacle in ArsR-based designs, was effectively eliminated by driving high-level expression of ArsR from the strong constitutive promoter PJ23119, yielding the parental plasmid pJ23119-K12. Arsenic is a significant environmental water pollutant, and detailed water quality arsenic limits have been established worldwide (Table S3). The sensor can detect As(III) at nanomolar levels, below the regulatory limits outlined in Table S3. Notably, however, this construct responds appreciably to Sb(III), especially at elevated concentrations closer to the environmental limits for antimony (Table S4). Mitigating this non-specific response has remained a critical, yet unresolved, challenge.

Recently, the *ant* operon of *Comamonas testosteroni* JL40 was identified as the first microbial resistance system specifically up-regulated by Sb(III) [29]. The operon comprises three genes: *antR*, encoding an ArsR/SmtB-family metalloregulator; *antA*, encoding a P-type ATPase that extrudes Sb(III); and *antC*, encoding a metallochaperone that sequesters intracellular Sb(III) and delivers it to AntA, thereby enhancing efflux efficiency [30].

To attenuate Sb(III)-mediated false positives in pJ23119-K12, we systematically incorporated *ant* operon components—individually and in combination—into the ArsR-based sensing chassis (Fig. 2). First, *antA* and *antC* were individually cloned downstream of the moderate constitutive promoter P*ceuR*, yielding pJ23119-antA and pJ23119-antC, respectively. A bicistronic *antA–antC*

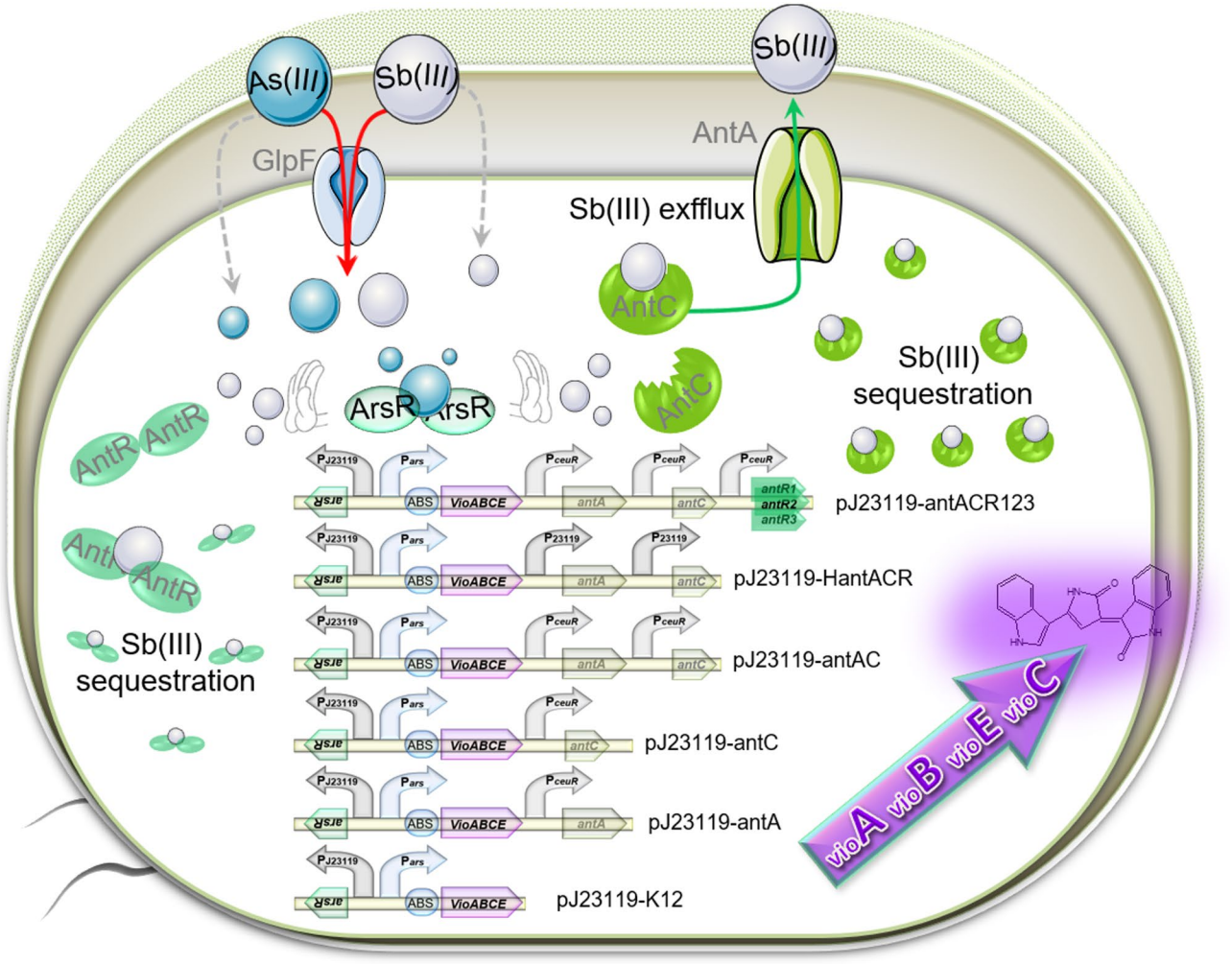

Fig. 2 Strategy for reducing Sb(III) cross-reactivity in ArsR-based biosensors. Components of the Sb(III)-responsive *ant* operon from *C. testosteroni* JL40—AntA (P-type ATPase), AntC (metallochaperone), and AntR (regulator)—were introduced individually or in combination to promote intracellular Sb(III) sequestration and efflux, thereby diminishing Sb(III)-induced activation of the DV reporter

cassette was then inserted to create pJ23119-antAC to couple Sb(III) sequestration with active efflux. To test the impact of elevated efflux capacity, the P*ceuR* promoter in pJ23119-antAC was replaced with the strong PJ23119 promoter, generating pJ23119-HAntAC. Finally, recognizing that dimeric AntR binds Sb(III) with high selectivity, we co-expressed AntR homologs (AntR1, AntR2, and AntR3) downstream of the *antA–antC* module, yielding pJ23119-antACR1, pJ23119-antACR2, and pJ23119-antACR3. Intracellular accumulation of these AntR variants is expected to scavenge free Sb(III), thereby reducing its availability to ArsR and minimizing off-target activation of the *vioABCE* reporter.

Impact of individual or combined AntA and AntC expression on biosensor performance

Next, we compared the As(III) and Sb(III) response profiles of the parental sensor TOP10/pJ23119-K12 with its derivatives carrying individual or combined *ant* components. All engineered strains retained robust As(III) responsiveness, exhibiting sigmoidal dose–response curves comparable to the parental construct (Fig. 3A). Non-linear regression (Fig. 3B) revealed excellent fits within the following ranges: 73 nM–4.688 μM for TOP10/pJ23119-antA and TOP10/pJ23119-antC (R^2 = 0.999 and 0.996, respectively) and 73 nM–2.344 μM for TOP10/pJ23119-antAC (R^2 = 0.990). However, introduction of *antA* or *antC*, alone or together, modestly increased the LOD for As(III) to 0.018 μM and narrowed the quantitative range (Fig. 3C). This increase in LOD and narrowing of the quantitative range may be attributed to the inherent properties of the *ant* operon and its components. While the *ant* operon is primarily found for antimonite resistance through AntC-mediated sequestration and AntA-mediated efflux [29, 30], the fact that antimony and arsenic are both Group 15 metalloids suggests that the *ant* operon components may not absolutely distinguish between these two elements. It is plausible that the introduction of *antAC* could also reduce the bioavailability of As(III), thereby decreasing the sensitivity of arsenite detection. The extent of this reduction is likely related to the expression levels of AntAC, as higher expression levels could potentially lead to greater interference with As(III) detection, such as in TOP10/pJ23119-HAntAC (Fig. 3A). When we attempted to quantify the intracellular concentrations of As(III) and Sb(III) using ICP-MS, we encountered difficulties due to the expression of the hydrophobic pigment DV. Its hydrophobic nature caused it to aggregate, compromising the integrity of the bacterial cells, making it impossible to accurately measure the intracellular metal ion concentrations. However, previous studies have shown that introducing AntAC reduces the intracellular concentration of Sb(III) but not As(III) or other metals [29, 31]. The high expression of AntAC in TOP10/pJ23119-HAntAC may impose a significant metabolic burden on the cells. The overexpression of AntAC indeed has a minor efflux effect on As(III), an effect that might be masked when AntAC is expressed at lower levels. Future work could involve upregulating AntAC expression independently in bacterial cells to examine changes in intracellular As(III) concentrations.

AntA and AntC drastically altered the Sb(III) response as intended. Both single-gene constructs (TOP10/pJ23119-antA and TOP10/pJ23119-antC) attenuated the DV signal elicited by Sb(III), slightly increasing the LOD (from 0.146 μM of the parental sensor to 0.293 μM). Strikingly, the AntAC co-expression strain shifted the Sb(III) LOD fourfold higher to 0.586 μM and markedly suppressed pigment accumulation. We hypothesized that increasing the expression levels of AntAC would further reduce Sb(III) interference. To this end, we replaced the constitutive P*ceuR* promoter driving *antAC* with the strong PJ23119 promoter to enhance AntAC expression. As anticipated, overexpression of AntAC under the strong PJ23119 promoter (TOP10/pJ23119-HAntAC) significantly reduced the Sb(III) response (Fig. 3D), but this also led to a significant increase in the As(III) LOD from 0.018 μM to 0.293 μM (Fig. 3C). Collectively, these data demonstrate that combined AntA and AntC expression effectively mitigates Sb(III) cross-reactivity. Nevertheless, this enhancement in Sb(III) resistance comes at the cost of slightly compromised As(III) sensitivity, as evidenced by the elevated LOD. Despite this trade-off, the sensor maintains robust As(III) responsiveness within a slightly compressed dynamic range. The underlying reason for this compromise is likely because the *ant* operon and its components, while highly specific for Sb(III), cannot perfectly distinguish between As(III) and Sb(III) [29, 32].

Based on this balanced performance, TOP10/pJ23119-antAC was selected as the optimal platform for further genetic refinement, including intracellular Sb(III) sequestration via AntR homologs. This choice was further validated by the subsequent integration of AntR, which preserved the enhanced Sb(III) resistance and unexpectedly increased the As(III) signal, thereby broadening the dynamic range and improving the overall sensitivity of the biosensor. These findings highlight the synergistic impact of AntA, AntC, and AntR on As(III)-specific signaling, as detailed in the following section.

Synergistic impact of AntA, AntC, and AntR on As(III)-specific signaling

All AntR-expressing derivatives retained the typical bell-shaped As(III) dose–response curves (Fig. 4A). Compared with the parent strain TOP10/pJ23119-antAC, the constructs TOP10/pJ23119-antACR1 and TOP10/pJ23119-antACR2 produced markedly stronger DV

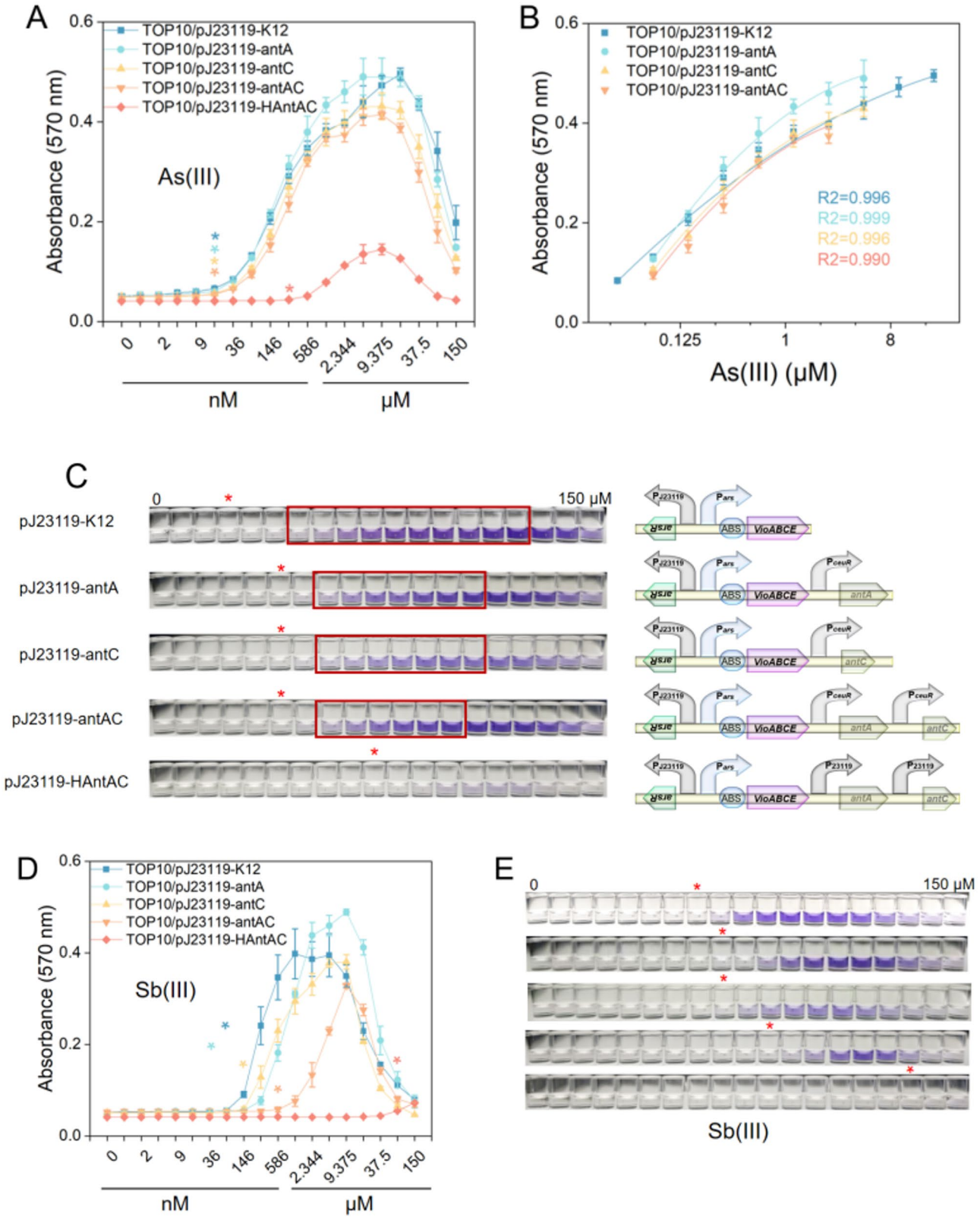

Fig. 3 Comparative performance of parental and engineered biosensors. **A** Dose–response curves for As(III) (log_2-transformed concentrations. **B** Regression analyses with indicated R^2 values. **C** Genetic schematics and representative n-butanol extracts showing DV accumulation. **D** Sb(III) dose–responses and **E** corresponding extracts. Multicolored stars indicate statistical significance compared to the unexposed control group. Red stars denote LODs, and red boxes highlight regression intervals. The raw data used to generate this figure are detailed in Tables S5 and S6

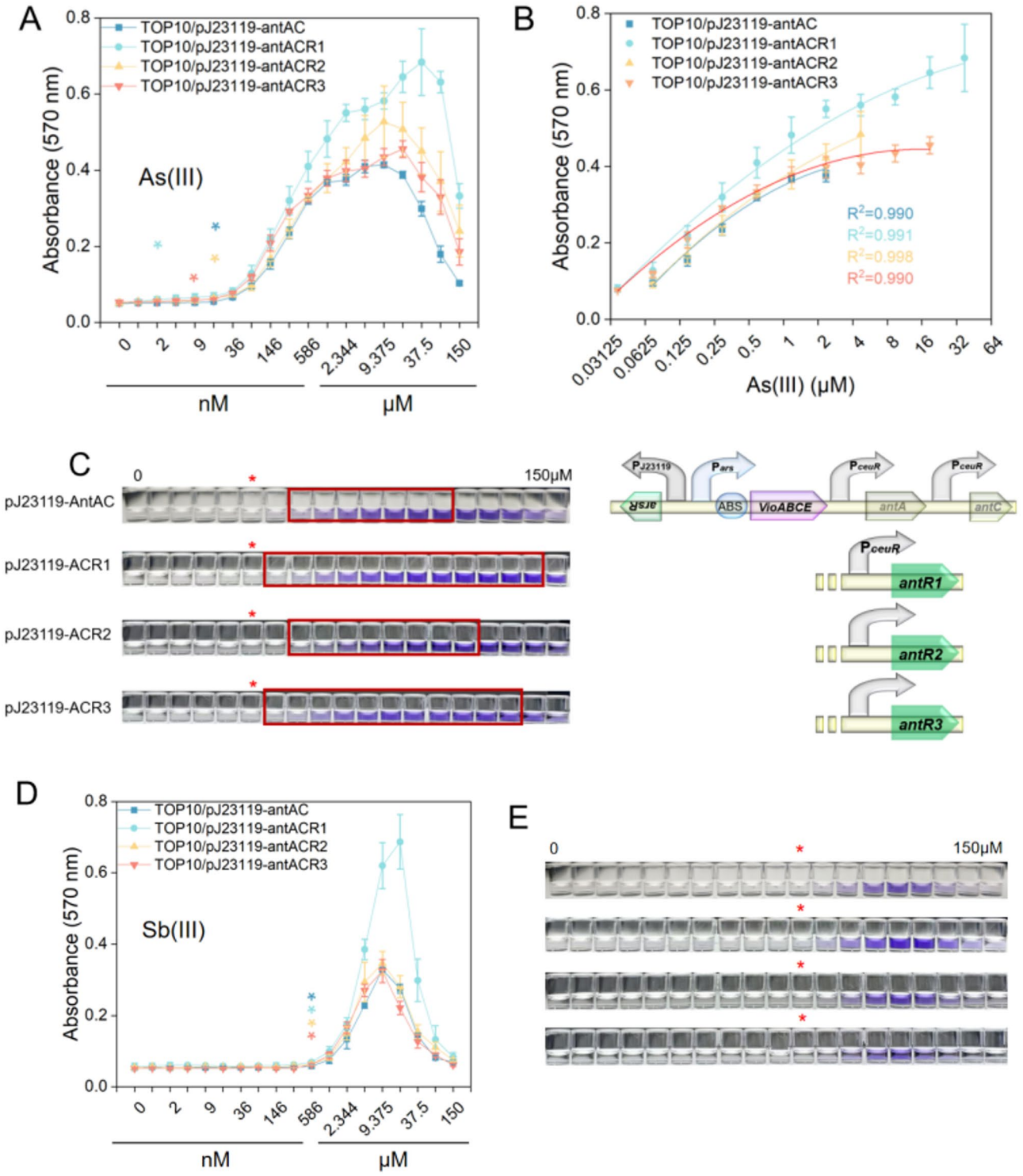

Fig. 4 Comparative performance of AntR-containing biosensors. **A** As(III) dose–response curves. **B** Regression analyses; red stars indicate LODs; red boxes denote linear ranges. **C** Representative n-butanol extracts for As(III) exposure. **D** Sb(III) dose–response curves and **E** corresponding extracts. Multicolored stars indicate statistical significance. Red stars denote LODs, and red boxes highlight regression intervals. The raw data used to generate this figure are detailed in Tables S7 and S8

signals, with antACR1 showing the most pronounced amplification.

Quantitative regression analyses (Fig. 4B) revealed that the parental sensor exhibited a maximum response at 9.375 μM As(III) and a linear range of 73 nM–2.344 μM (R^2 = 0.990). Introducing the AntR1 sequestration module shifted the peak response to 37.5 μM and extended the linear range to 36 nM–37.5 μM (R^2 = 0.991). AntR2 preserved the peak at 9.375 μM but widened the range to 73 nM–4.688 μM (R^2 = 0.998), whereas AntR3 shifted the peak to 18.75 μM and provided a wide range of 36 nM–18.75 μM (R^2 = 0.990). Despite these shifts, the LOD for As(III) remained unchanged.

Although AntR homologs were intended solely to sequester Sb(III), their intracellular accumulation unexpectedly amplified As(III) signaling, broadening the dynamic range. It suggests a direct or indirect interaction between AntR and the ArsR–P*ars* regulatory circuit. Potential mechanisms for this interaction could include operator sequence overlap or co-binding of AntR with the promoter regions affecting vio*ABCE* expression, which could modulate the transcriptional activity of the ArsR repressor. Surprisingly, antACR2 and antACR3 displayed Sb(III) response curves almost superimposable on that of antAC (Fig. 4D), whereas antACR1 exhibited a higher Sb(III)-induced signal (Fig. 4E). Importantly, the Sb(III) LOD for all three constructs remained 0.586 μM—identical to antAC—indicating that AntR sequestration alone does not further suppress Sb(III) interference within the tested concentration window.

These data demonstrate that AntR integration enhances As(III) sensitivity and widens the quantitative range without compromising Sb(III) specificity. The unexpected amplification of the As(III) signal by AntR1 suggests potential interactions that could impact the redox state, create transcriptional competition, or interfere with ArsR dimerization. These mechanisms require further investigation to clarify the role of AntR in modulating the ArsR regulatory circuit. Future studies could examine these interactions in detail, enhancing our understanding of the regulatory dynamics. Among the variants, TOP10/pJ23119-antACR1 was selected for subsequent environmental validation owing to its superior signal amplification and extended linearity. The excellent selectivity of this construct, as detailed in the following section, underscores its potential for robust and specific arsenite detection in complex environmental samples.

Selectivity and interference resistance of TOP10/pJ23119-antACR1

The optimized biosensor TOP10/pJ23119-antACR1 was challenged with three sub-cytotoxic concentrations of Mg(II), Cd(II), Hg(II), Mn(II), Pb(II), Cu(II), Sb(III), and As(III). Only As(III) elicited a pronounced DV signal. All divalent metal ions behaved indistinguishably from the blank (Fig. 5A). Sb(III) at 1.2 and 2.4 μM induced a minor but statistically significant pigment increase (Fig. 5A), yet the color remained visually subtle (Fig. 5B). No visible purple was observed for any metal other than As(III), confirming the high selectivity of the sensor.

To assess potential interference under realistic conditions, the biosensor was co-exposed to 0.15 μM As(III) in the presence of 0.5 or 1 μM of each interfering metal. Neither bacterial growth (Fig. 5C) nor As(III)-dependent DV production was affected ($P > 0.05$; Fig. 5D). Even 1 μM Sb(III)—a concentration rarely encountered in environmental samples—did not compromise As(III) detection, likely because dimeric ArsR exhibits a higher affinity for As(III) than for Sb(III). Extracts from all As(III)-free mixtures remained colorless and were statistically distinct from the As(III)-positive control ($P < 0.0001$; Fig. 5E).

The decision to exclude Bi(III) and As(V) from our testing was informed by the extensive literature on ArsR-based biosensors, which uniformly identifies Sb(III) as the principal source of cross-reactivity [6, 16]. High Bi(III) and As(V) concentrations have been documented to cause interference primarily at levels in the tens of micromolar range [11, 33]. Meanwhile, phosphate and other anions are more likely to influence the bioavailability of As(III) rather than directly interfere with the biosensor [34, 35]. Collectively, TOP10/pJ23119-antACR1 exhibits high selectivity for As(III), tolerates environmentally relevant concentrations of co-occurring metals, and shows negligible interference from Sb(III) except at supra-environmental levels (refer to Table S4, which outlines regulatory limits for antimony in water quality standards and guidelines worldwide). These findings highlight its suitability for field deployment and have prompted further validation in authentic environmental water matrices.

Environmental validation of TOP10/pJ23119-antACR1

To evaluate the real-world applicability of TOP10/pJ23119-antACR1, we tested its performance in four environmental water matrices: deionized water, municipal tap water, surface water from Donghu Park, and seawater from Daya Bay. Contrary to most whole-cell biosensors that employ only 10–20% (v/v) matrix, we established 90% freshwater and 50% seawater formulations (Table 2) to minimize dilution-related LOD increases while sustaining robust bacterial growth and pigment expression.

Cell density remained stable in all matrices (Fig. 6A). Seawater cultures exhibited marginally lower OD_{600}, consistent with osmotic stress [36]. Nevertheless, clear dose–response relationships were observed for As(III) in every matrix (Fig. 6B). High dissolved organic carbon in surface water [37] did not impair the signal, and seawater

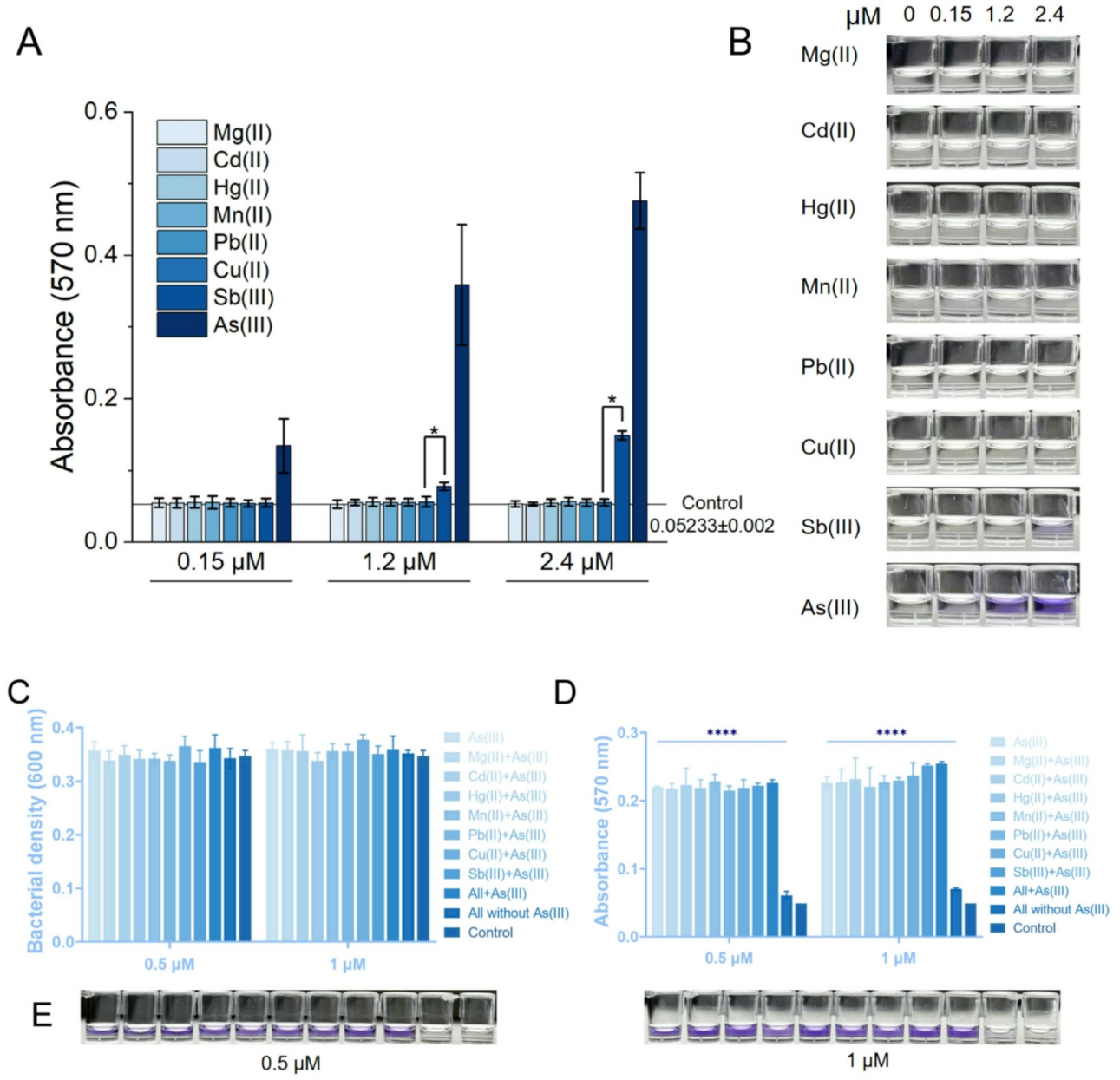

Fig. 5 Selectivity and interference resistance of TOP10/pJ23119-antACR1. **A** DV signal intensities upon exposure to individual metals at three concentrations. Horizontal line indicates blank control. (*$P < 0.05$). **B** Representative n-butanol extracts. **C**–**E** Co-exposure assays: bacterial growth (**C**), DV production (**D**), and visual extracts (**E**) in the presence of 0.15 μM As(III) plus 0.5 or 1 μM interfering metals. (****$P < 0.0001$). The raw data used to generate this figure are detailed in Tables S9, S10, and S11

salinity did not abolish As(III)-dependent DV synthesis. However, absolute absorbance was slightly reduced. All matrices displayed excellent technical reproducibility, with a slight inter-replicate colorimetric variability indistinguishable to the naked eye (Fig. 6C), underscoring the sensor's quantitative robustness and visual reliability.

Linear regression over 0–2.5 μM As(III) yielded strong correlations (R^2 >0.99) for deionized water, tap water, surface water, and seawater (Fig. 6D). The simplicity of the readout—purple intensity visible to the naked eye—supports low-cost, high-throughput screening without specialized instrumentation. To further evaluate the accuracy and practical applicability of the biosensor, we spiked three types of environmental water samples (tap water, surface water, and seawater) with 0.2 and 0.6 μM As(III). We compared the detection results obtained using the biosensor and atomic fluorescence spectrometry (AFS). As shown in Fig. 6E, the biosensor detection results were in good agreement with those obtained by AFS, demonstrating the reliability of the biosensor

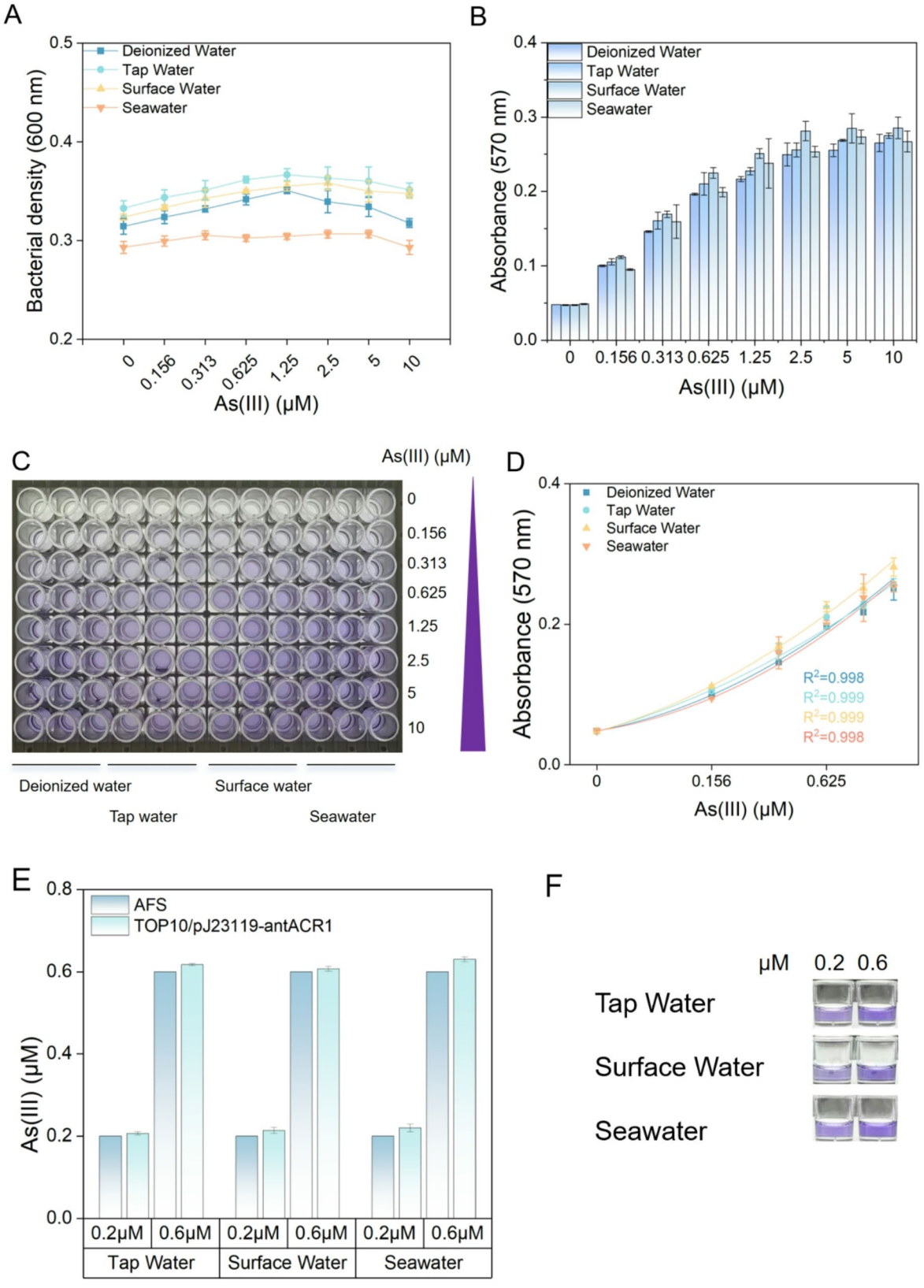

Fig. 6 (See legend on next page.)

(See figure on previous page.)

Fig. 6 Performance of TOP10/pJ23119-antACR1 in environmental water matrices. **A** Bacterial growth under escalating As(III) concentrations. **B** Dose–response curves. **C** Representative n-butanol extracts. **D** Linear regression of As(III) versus DV signal for each matrix. **E** Comparison of biosensor detection and AFS measurements for environmental water samples spiked with 0.2 and 0.6 μM As(III). **F** Representative n-butanol extracts from biosensor detection of environmental water samples spiked with 0.2 and 0.6 μM As(III). Experiments were conducted in at least three independent biological replicates, and results are presented as mean ± standard deviation (SD). The raw data used to generate this figure are detailed in Tables S12 and S13

method. The intensity of the purple pigment signal, which is visible to the naked eye, further supports the feasibility of low-cost, high-throughput screening without the need for specialized instrumentation (Fig. 6F). These findings indicate that the biosensor developed in this study serves as a valuable complement to instrumental analytical methods. Future work should further test the biosensor in more chemically diverse real-world samples, such as wastewater and mining effluent, to assess its robustness and applicability in varied environmental conditions.

Crosstalk between distinct metal-resistance systems has proven effective for enhancing sensor specificity, as demonstrated by CadC/CadR co-employment for Cd(II) [38] and *pbr–cad–mer* operon fusion for Pb(II)/Cd(II)/Hg(II) discrimination [21, 39]. Here, we repurposed the Sb(III)-selective *ant* operon to suppress Sb(III) interference in an ArsR-based As(III) sensor. While Sb(III) reactivity was not eliminated, it became significant only at concentrations far exceeding environmental levels. Table S4 details regulatory limits for antimony in water quality standards and guidelines worldwide, ensuring a negligible impact on field applications.

Unexpectedly, AntR homolog co-expression intensified As(III) signaling and extended the quantitative range. This phenomenon suggests that AntR may modulate ArsR–P*ars* dynamics through several potential mechanisms. One possibility is that AntR interacts allosterically with ArsR, altering its conformation and thereby reducing its affinity for the Pars promoter. Alternatively, AntR might bind competitively to the P*ars* promoter region, preventing ArsR from binding and derepressing the *vioABCE* operon. Another potential mechanism is that AntR influences DNA topology, which could affect the binding efficiency of ArsR to its operator sites. Unlike AntC, which primarily functions in the sequestration of Sb(III), AntR's effect on As(III) signaling suggests a more complex regulatory role. Future mechanistic studies are warranted to decipher the precise interplay between the *ant* and *ars* operons. Elucidating these interactions will guide the development of next-generation Group 15 metalloid sensors with superior As(III) selectivity and broader environmental relevance.

Conclusions

We report the rational engineering of a selective As(III) whole-cell biosensor by grafting the Sb(III)-specific ant resistance module onto an ArsR-based deoxyviolacein reporter chassis. Co-expression of the P-type ATPase AntA and the metallochaperone AntC lowered the Sb(III) detection limit fourfold (from 0.073 to 0.586 μM). These modifications almost abolished pigment accumulation at environmentally relevant antimony concentrations (typically below 50 nM, as detailed in Table S4), while preserving robust As(III) responsiveness (LOD = 18 nM). Further incorporation of the metalloregulator AntR1 unexpectedly amplified the As(III) signal and widened the linear range to 36 nM–37.5 μM (R^2 = 0.991), yielding the optimized strain TOP10/pJ23119-antACR1. The final sensor discriminates As(III) from various divalent heavy metals and tolerates up to 1 μM Sb(III) without losing accuracy. Validation in 90% freshwater and 50% seawater matrices demonstrated quantitative As(III) recovery within 0–2.5 μM, confirming compatibility with municipal tap, surface, and marine samples. These results demonstrate that the *ant–ars* cross-operon assembly is a promising approach for enhancing selectivity towards As(III) over other Group 15 metalloids, such as Sb(III), and underscore the potential of TOP10/pJ23119-antACR1 as a low-cost, high-throughput tool for environmental arsenic surveillance.

Supplementary Information

The online version contains supplementary material available at https://doi.org/10.1186/s12934-025-02865-z.

Supplementary Material 1.

Author contributions

Jingwen Ling: Investigation, Data curation. Yan Guo: Formal analysis, Writing—review & editing, Funding acquisition. Mingqi Liu: Investigation. Jianpei Yun: Software, Methodology. Boxin Li: Resources. Xueqin Yang: Data curation. Xuli Wu: Supervision. Chang-ye Hui: Project administration, Conceptualization, Methodology, Writing—original draft, Funding acquisition.

Funding

This work was supported by the Natural Science Foundation of Shenzhen Municipality (JCYJ20230807151400002, JCYJ20240813162259005), the Natural Science Foundation of Guangdong Province (2023A1515011184, 2025A1515011667) and Shenzhen Key Medical Discipline Construction Fund (SZXK068).

Data availability

All the data of this study contained in the manuscript and further data can be obtained related to this study from Corresponding authors.

Declarations

Ethics approval and consent to participate

Not applicable.

Consent for publication
All authors consent to the publication of this manuscript in its submitted form.

Competing interests
The authors declare no competing interests.

Author details
[1]School of Public Health, Shenzhen University Medical School, Shenzhen University, Shenzhen, Guangdong 518055, China
[2]Shenzhen Prevention and Treatment Center for Occupational Diseases, Shenzhen 518020, China
[3]School of Public Health, Guangdong Medical University, Dongguan 523808, China

Received: 28 July 2025 / Accepted: 27 October 2025
Published online: 24 November 2025

References

1. Patel KS, Pandey PK, Martin-Ramos P, Corns WT, Varol S, Bhattacharya P, Zhu Y. A review on arsenic in the environment: bio-accumulation, remediation, and disposal. RSC Adv. 2023;13:14914–29.
2. Podgorski J, Berg M. Global threat of arsenic in groundwater. Science. 2020;368:845–50.
3. Garla R, Ganger R, Mohanty BP, Verma S, Bansal MP, Garg ML. Metallothionein does not sequester arsenic(III) ions in condition of acute arsenic toxicity. Toxicology 2016, 366(7):68–73.
4. Shakoor MB, Niazi NK, Bibi I, Shahid M, Saqib ZA, Nawaz MF, Shaheen SM, Wang H, Tsang DCW, Bundschuh J, et al. Exploring the arsenic removal potential of various biosorbents from water. Environ Int. 2019;123:567–79.
5. Ma J, Sengupta MK, Yuan D, Dasgupta PK. Speciation and detection of arsenic in aqueous samples: a review of recent progress in non-atomic spectrometric methods. Anal Chim Acta. 2014;831:1–23.
6. Hui CY, Liu MQ, Guo Y. Synthetic bacteria designed using Ars operons: a promising solution for Arsenic biosensing and bioremediation. World J Microbiol Biotechnol. 2024;40:192.
7. Bereza-Malcolm L, Aracic S, Mann G, Franks AE. The development and analyses of several Gram-negative arsenic biosensors using a synthetic biology approach. Sens Actuators B. 2018;256:117–25.
8. Fernandez M, Morel B, Ramos JL, Krell T. Paralogous regulators ArsR1 and ArsR2 of Pseudomonas Putida KT2440 as a basis for arsenic biosensor development. Appl Environ Microbiol. 2016;82:4133–44.
9. Kaur H, Kumar R, Babu JN, Mittal S. Advances in arsenic biosensor development–a comprehensive review. Biosens Bioelectron. 2015;63:533–45.
10. Hui CY, Guo Y, Liu L, Zhang NX, Gao CX, Yang XQ, Yi J. Genetic control of Violacein biosynthesis to enable a pigment-based whole-cell lead biosensor. RSC Adv. 2020;10:28106–13.
11. Guo Y, Liu M, Xq Y, Yy G, Cy H. Optimized genetic circuitry and reporters for sensitive whole-cell arsenic biosensors: advancing environmental monitoring. Appl Environ Microbiol 2025;91:e00601-25.
12. Guo Y, Hu SY, Wu C, Gao CX, Hui CY. Biosynthesis of Indigo dyes and their application in green chemical and visual biosensing for heavy metals. ACS Omega. 2024;9:33868–81.
13. Liu MQ, Guo Y, Wu C, Gao CX, Liu F, Hui CY. Visual arsenic detection in environmental waters: innovating with a naked-eye biosensor for universal application. J Hazard Mater. 2024;477:135398.
14. Chen X, Yao H, Song D, Lin J, Zhou H, Yuan W, Song P, Sun G, Xu M. A novel antimony-selective ArsR transcriptional repressor and its specific detection of antimony trioxide in environmental samples via bacterial biosensor. Biosens Bioelectron. 2023;220:114838.
15. Fang Y, Zhu C, Chen X, Wang Y, Xu M, Sun G, Guo J, Yoo J, Tie C, Jiang X, Li X. Copy number of ArsR reporter plasmid determines its arsenite response and metal specificity. Appl Microbiol Biotechnol. 2018;102:5753–61.
16. Chen SY, Zhang Y, Li R, Wang B, Ye BC. De Novo design of the ArsR regulated P_{ars} promoter enables a highly sensitive whole-cell biosensor for arsenic contamination. Anal Chem. 2022;94:7210–8.
17. Chen SY, Wei W, Yin BC, Tong Y, Lu J, Ye BC. Development of a highly sensitive whole-cell biosensor for arsenite detection through engineered promoter modifications. ACS Synth Biol. 2019;8:2295–302.
18. Prabaharan C, Kandavelu P, Packianathan C, Rosen BP, Thiyagarajan S. Structures of two ArsR As(III)-responsive transcriptional repressors: implications for the mechanism of derepression. J Struct Biol. 2019;207:209–17.
19. Guo M, Chen X, Chen S, Su H, Liu H, Xie G, Sun B. Replacing manual operation with bio-automation: A high-throughput evolution strategy to construct an integrated whole-cell biosensor for the simultaneous detection of Methylmercury and mercury ions without manual sample digestion. J Hazard Mater. 2024;465:133492.
20. Hu S-y, Hui C-y, Wu C, Gao C-x, Huang Z, Guo Y. Dual-colored bacterial biosensor responsive to cadmium, mercury, and lead for detecting heavy metal pollution in seawater. Ecol Indic. 2024;166:112244.
21. Guo Y, Zhu D-L, Liu M-Q, Chen Y-T, Hu S-Y, Hui C-Y. Metabolic engineering-enabled dual-color biosensor for discriminative and sensitive detection of toxic lead and mercury in environmental waters. J Environ Chem Eng. 2024;12:114178.
22. He MY, Lin YJ, Kao YL, Kuo P, Grauffel C, Lim C, Cheng YS, Chou HD. Sensitive and specific cadmium biosensor developed by reconfiguring metal transport and leveraging natural gene repositories. ACS Sens. 2021;6:995–1002.
23. Guo M, Du R, Xie Z, He X, Huang K, Luo Y, Xu W. Using the promoters of MerR family proteins as rheostats to engineer whole-cell heavy metal biosensors with adjustable sensitivity. J Biol Eng. 2019;13:70.
24. Hui CY, Guo Y, Zhu DL, Li LM, Yi J, Zhang NX. Metabolic engineering of the Violacein biosynthetic pathway toward a low-cost, minimal-equipment lead biosensor. Biosens Bioelectron. 2022;214:114531.
25. Ma BC, Guo Y, Lin YR, Zhang J, Wang XQ, Zhang WQ, Luo JG, Chen YT, Zhang NX, Lu Q, Hui CY. High-throughput screening of human mercury exposure based on a low-cost naked eye-recognized biosensing platform. Biosens Bioelectron. 2024;248:115961.
26. Guo Y, Wu C, Hu SY, Xie YX, Wu WY, Li BX, Chen YT, Hui CY. ChpR-displaying bacteria for bioremediation of Chlorpyrifos and TCP: A whole-cell biosorbent approach. Water Res. 2025;283:123775.
27. Liu XY, Guo Y, Zhang WQ, Bai J, Ma BC, Zhou LT, Hui CY. Bridging the mercury exposure threshold: development and application of whole-cell biosensors incorporating biotransformation pathways. Environ Res. 2025;275:121418.
28. Zhang J, Guo Y, Lin YR, Ma BC, Ge XR, Zhang WQ, Zhang NX, Yang SM, Hui CY. Detection of cadmium in human biospecimens by a cadmium-selective whole-cell biosensor based on Deoxyviolacein. ACS Biomater Sci Eng. 2024;10:4046–58.
29. An L, Luo X, Wu M, Feng L, Shi K, Wang G, Rosen BP, Li M. Comamonas testosteroni AntA encodes an antimonite-translocating P-type ATPase. Sci Total Environ. 2021;754:142393.
30. An L, Xu M, Hong M, Zhao L, Wei A, Luo X, Shi K, Zheng S, Li M. A novel antimony metallochaperone AntC in Comamonas testosteroni JL40 and its application in antimony immobilization. Sci Total Environ. 2024;911:168815.
31. Luo X, Guo J, Lan Y, An L, Zhang X, Shi K, Zheng S, Li M. Toxic response of antimony in the Comamonas testosteroni and its application in soil antimony bioremediation. Environ Int. 2023;178:108040.
32. Viswanathan T, Chen J, Wu M, An L, Kandavelu P, Sankaran B, Radhakrishnan M, Li M, Rosen BP. Functional and structural characterization of AntR, an Sb(III) responsive transcriptional repressor. Mol Microbiol. 2021;116:427–37.
33. Liao VH, Ou KL. Development and testing of a green fluorescent protein-based bacterial biosensor for measuring bioavailable arsenic in contaminated groundwater samples. Environ Toxicol Chem. 2005;24:1624–31.
34. Monroy-Licht A. Effect of phosphate on arsenic species uptake in plants under hydroponic conditions. J Plant Res. 2023;136:729–42.
35. Corrales D, Alcantara C, Clemente MJ, Velez D, Devesa V, Monedero V, Zuniga M. Phosphate uptake and its relation to arsenic toxicity in lactobacilli. Int J Mol Sci 2024; 25:5017.
36. Wu C, Guo Y, Xie YX, Hu SY, Ou JM, Li BX, Zhang NX, Hui CY. Visual signal transduction for environmental stewardship: A novel biosensing approach to identify and quantify chlorpyrifos-related residues in aquatic environments. J Hazard Mater. 2024;480:136213.
37. Hui C-y, Guo Y, Gao C-x, Li H, Lin Y-r, Yun J-p, Chen Y-t, Yi J. A tailored indigoidine-based whole-cell biosensor for detecting toxic cadmium in environmental water samples. Environ Technol Innov. 2022;27:102511.
38. Hui CY, Guo Y, Wu J, Liu L, Yang XQ, Guo X, Xie Y, Yi J. Detection of bioavailable cadmium by double-color fluorescence based on a dual-sensing bioreporter system. Front Microbiol. 2021;12:696195.

39. Hui CY, Guo Y, Li H, Chen YT, Yi J. Differential detection of bioavailable mercury and cadmium based on a robust dual-sensing bacterial biosensor. Front Microbiol. 2022;13:846524.

Publisher's Note

Springer Nature remains neutral with regard to jurisdictional claims in published maps and institutional affiliations.